Journal of Advanced Ceramics
2023, **12**(12): 2315–2330
https://doi.org/10.26599/JAC.2023.9220822
ISSN 2226-4108
CN 10-1154/TQ

Research Article

In-situ observation and mechanism of calcium–magnesium–alumina–silicate (CMAS) melts-induced degradation of RE_2SiO_5 (RE = Tb, Dy, Ho, Y, Er, Tm, and Yb) ceramics at 1500 °C

Zhilin Tian[a], Keyu Ming[a], Liya Zheng[a,*], Zhilin Chen[a], Fan Zhou[a], Peng Liu[a], Zihao Qiu[a], Donghui Wei[b], Bin Li[a,*], Jingyang Wang[c,*]

[a]*School of Materials*, *Shenzhen Campus of Sun Yat-sen University*, *Shenzhen 518107*, *China*
[b]*School of Metallurgy*, *Northeastern University*, *Shenyang 110819*, *China*
[c]*Shenyang National Laboratory for Materials Science*, *Institute of Metal Research*, *Chinese Academy of Sciences*, *Shenyang 110016*, *China*

Received: August 14, 2023; Revised: October 25, 2023; Accepted: October 26, 2023

Abstract: Rare earth (RE) silicate is one of the most promising environmental barrier coatings for silicon-based ceramics in gas turbine engines. However, calcium–magnesium–alumina–silicate (CMAS) corrosion becomes much more serious and is the critical challenge for RE silicate with the increasing operating temperature. Therefore, it is quite urgent to clarify the mechanism of high-temperature CMAS-induced degradation of RE silicate at relatively high temperatures. Herein, the interaction between RE_2SiO_5 and CMAS up to 1500 ℃ was investigated by a novel high-temperature *in-situ* observation method. High temperature promotes the growth of the main reaction product ($Ca_2RE_8(SiO_4)_6O_2$) fast along the [001] direction, and the precipitation of short and horizontally distributed $Ca_2RE_8(SiO_4)_6O_2$ grains was accelerated during the cooling process. The increased temperature increases the solubility of RE elements, decreases the viscosity of CMAS, and thus elevates the corrosion reaction rate, making RE_2SiO_5 fast interaction with CMAS and less affected by RE element species.

Keywords: calcium–magnesium–alumina–silicate (CMAS) corrosion; environmental barrier coating; rare earth (RE) silicate; high temperature

1 Introduction

Advanced SiC fiber-reinforced SiC ceramic matrix composites (SiC_f/SiC CMCs) promise enhanced energy efficiency for gas turbine engines due to substantially higher operation temperatures [1–3]. To extend lifetime and enhance tability of SiC_f/SiC CMCs, the environmental barrier coating (EBC) is quite crucial to protect them from corrosion by the combustion atmosphere [4,5]. Rare earth silicates are well known as the third generation of EBC candidates due to excellent water vapor corrosion resistance and matched thermal expansion coefficient [6–8], and the combination of SiC_f/SiC CMCs and rare earth silicate EBC is

* Corresponding authors.
E-mail: L. Zheng, zhengly26@mail.sysu.edu.cn;
B. Li, libin75@mail.sysu.edu.cn;
J. Wang, jywang@imr.ac.cn

extremely promising and expected to be used as hot section components in gas turbine engines [9].

However, since the eruption of Iceland's Eyjafjallajökull volcano in 2010, the corrosion of hot section components in gas turbine engines by CMAS molten melts has gradually attracted a lot of attention [10,11]. CMAS refers to the ingested airborne inorganic particles (sand, dust, and volcano ash) with the content of calcium–magnesium–alumina–silicates [11,12]. Therefore, it is necessary to know the interaction between CMAS and rare earth silicates, which has been widely investigated at 1300–1400 ℃ [13–23]. It has been revealed that complex corrosion processes can be divided into three stages [24]. Rare earth silicates first dissolve into CMAS. Then, $Ca_2RE_8(SiO_4)_6O_2$ will precipitate when CMAS is saturated in $REO_{1.5}$. CMAS is gradually consumed leading to equilibrium with rare earth silicates and infiltration will slow down. Most rare earth silicates attacked by CMAS under 1300 ℃ follow the above corrosion behavior. Different rare earth silicates display diverse resistances to CMAS corrosion and RE elements are the key to regulating CMAS resistance. When CMAS interacted with RE_2SiO_5 ceramics at 1300 ℃, for X1-RE_2SiO_5, the width of the reaction zone increased as the radius of RE^{3+} decreased [18]. Conversely, the width of the reaction zone decreases with the reduction of the radius of RE^{3+} for X2-RE_2SiO_5 [25]. In addition, higher temperatures accelerate the degradation of rare earth silicates. For instance, a thick layer of $Ca_2RE_8(SiO_4)_6O_2$ accumulated between the residual CMAS and $RE_2Si_2O_7$ substrate when CMAS corroded $Yb_2Si_2O_7$ and $Lu_2Si_2O_7$ at 1300 ℃; and when temperature increases to 1500 ℃, intergranular infiltration of CMAS will occur and results in severe "blister" damage [26]. Therefore, composition and temperature have a significant influence on the CMAS resistance of rare earth silicates. However, most previous research focused on the interaction between a specific rare earth silicate ceramic and CMAS at 1300 ℃, and seldom investigations explore CMAS corrosion at 1500 ℃.

In recent years, the HfO_2–Si bond coat was developed to improve the temperature capability of EBC [27]. The upper use temperature can be up to 1482 ℃, which imposes harsh requirements on the performance of rare earth silicates. Since EBC surface temperatures are expected to be much higher (1500 ℃ and above), the CMAS attack of EBCs is expected to be amplified as all the relevant processes (diffusion, reaction, viscosity, etc.) are thermally activated [21]. EBCs are dense, and, therefore, it is preferred that they have low reactivity with the CMAS to retain the EBC's integrity. Rare earth silicates with good CMAS resistance above 1500 ℃ become urgent. Recently, some researchers have explored the CMAS corrosion of some RE_2SiO_5 such as $(Y_{1-x}Yb_x)_2SiO_5$ and Yb_2SiO_5 at 1500 ℃ [28,29]. More severe corrosion has been observed, but the factors affecting the high-temperature CMAS corrosion are not yet clear. In addition, *in-situ* observation of high-temperature CMAS-induced corrosion of rare earth silicate ceramics is still challenging, which is very important to clearly show the interaction between RE_2SiO_5 and CMAS, thereby guiding the EBC design. The lack of insight into the CMAS resistance at high temperatures (≥ 1500 ℃), especially for RE_2SiO_5 ceramics, limits applications of RE_2SiO_5 ceramics at higher temperatures.

In this work, the interactions of RE_2SiO_5 (RE = Tb, Dy, Ho, Y, Er, Tm, and Yb) with CMAS were firstly systematically investigated up to 1500 ℃. The phase composition and distribution of reaction products were analyzed to illustrate the corrosion mechanism. The *in-situ* observation was applied to further clarify the effect of the temperature and RE species on $Ca_2RE_8(SiO_4)_6O_2$ formation. CMAS infiltration in RE_2SiO_5 was observed by the characterization of cross-section and reaction front, and the resistance to CMAS of RE_2SiO_5 (RE = Tb, Dy, Ho, Y, Er, Tm, and Yb) was evaluated based on the analysis of CMAS infiltration depth. The results of this work systematically evaluated the high-temperature corrosion resistance of RE_2SiO_5 (RE = Tb, Dy, Ho, Y, Er, Tm, and Yb) and also provided important guidelines for the design of RE_2SiO_5 EBC.

2 Experimental

2.1 Preparation of RE_2SiO_5 (RE = Tb, Dy, Ho, Y, Er, Tm, and Yb) ceramics

Bulk RE_2SiO_5 (RE = Tb, Dy, Ho, Y, Er, Tm, and Yb) ceramics were fabricated by the solid-state sintering method. The starting materials, i.e., RE_2O_3 (RE = Dy, Ho, Y, Er, Tm, and Yb), Tb_4O_7 (Guangzhou Jianfeng Rare Earth Material Co., Ltd., > 99.9%), and SiO_2 (Sinopharm Chemical Reagent Co., Ltd., 99.7%) were first heated at 1000 ℃ for 1 h to remove the moisture. Then, they were ball milled according to the

stoichiometric ratio of RE_2SiO_5 with zirconia balls in ethanol for 12 h. After drying and sieving, the mixtures were placed in an Al_2O_3 crucible and pressureless sintered at 1550 ℃ for 1.5 h to achieve pure RE_2SiO_5 powders. Before the as-prepared powders were pressed into a disc of 13 mm in diameter and cold isostatic pressed at 200 MPa for 15 min, they were ball-milled again to refine the particle size. At last, the RE_2SiO_5 green bodies were sintered at 1550 ℃ for 10 h to obtain bulk and dense ceramics.

2. 2 CMAS corrosion test

CMAS with a composition of $33CaO–9MgO–13AlO_{1.5}–45SiO_2$ was used in this work. CaO (Shanghai Macklin Biochemical Co., Ltd., 98%), MgO (Shanghai Macklin Biochemical Co., Ltd., 99.7%), Al_2O_3 (Shanghai Macklin Biochemical Co., Ltd., 99.8%), and SiO_2 (Sinopharm Chemical Reagent Co., Ltd., 99.7%) were weighed according to the molar ratio and mixed by ball milling in ethanol. The mixtures were then dried and calcined in a muffle furnace at 1200 ℃ for 24 h below its melting point. Then the obtained materials were re-grounded into fine powders. For the corrosion test, the CMAS powders were mixed with ethanol to obtain a slurry and coated on the surface of RE_2SiO_5. After several times of drying and coating, the loading of the CMAS powders were kept at 35 mg/cm^2. Then CMAS corrosion tests were conducted at 1500 ℃ in a muffle furnace for different durations. After the corrosion test, the surface morphology, cross-section microstructure, and the phase composition of the sample were characterized.

2. 3 Characterizations

An X-ray diffractometer (PANalytical Empyrean, Almero, the Netherlands) was used to confirm the phase composition. Microstructure and composition were analyzed by a scanning electron microscope (SEM; SIGMA 300, ZEISS, Germany) with energy-dispersive X-ray spectrometry (EDS). Surface morphologies of RE_2SiO_5 (RE = Tb, Dy, Ho, Y, Er, Tm, and Yb) after CMAS corrosion were characterized by an ultra-depth of field microscope (DVM6M, Leica, Germany). The high-temperature contact angle measurements of CMAS were performed by a homemade high-temperature contact angle tester. The temperature-dependent viscosity was calculated by the FactSage software.

3 Results

Figure 1 shows X-ray diffraction (XRD) patterns of as-prepared RE_2SiO_5 (RE = Tb, Dy, Ho, Y, Er, Tm, and Yb). Their X-ray diffraction peaks shift to a high angle with the reduction of RE^{3+} radius. Most of RE_2SiO_5 are pure phases, and only a tiny amount of $RE_2Si_2O_7$ impurities were detected in Tm_2SiO_5 and Yb_2SiO_5. The microstructures of RE_2SiO_5 (RE = Tb, Dy, Ho, Y, Er, Tm, and Yb) are presented in Fig. 2, wherein they all exhibit equiaxed grains, and the average grain sizes are 1.6–2.9 μm. Y_2SiO_5 possesses the largest grain size among all the as-prepared RE_2SiO_5 (RE = Tb, Dy, Ho, Y, Er, Tm, and Yb). Moreover, seldom pores can be detected on the surface of RE_2SiO_5, and the samples are more than 92% of theoretical density. The successful preparation of bulk and dense RE_2SiO_5 (RE = Tb, Dy, Ho, Y, Er, Tm, and Yb) lays a foundation for the investigation of their CMAS resistance at high temperatures.

The interactions between CMAS and RE_2SiO_5 (RE = Tb, Dy, Ho, Y, Er, Tm, and Yb) conducted at 1500 ℃ for different times were investigated. Figure 3 shows XRD patterns of RE_2SiO_5 (RE = Tb, Dy, Ho, Y, Er, Tm, and Yb) after CMAS corrosion at 1500 ℃ for 5 h. $Ca_2RE_8(SiO_4)_6O_2$ can be detected on the surface of all RE_2SiO_5. The intensity of (200) and (300) diffraction peaks of $Ca_2RE_8(SiO_4)_6O_2$ (RE = Tb, Dy, Ho, Y, Er, Tm, and Yb) are much stronger than that of others which suggests high exposure of (100) facet.

Figure 4 presents the surface microstructures of RE_2SiO_5 (RE = Tb, Dy, Ho, Y, Er, Tm, and Yb) after CMAS corrosion at 1500 ℃ for 5 h. A large number of long rod-like $Ca_2RE_8(SiO_4)_6O_2$ grains are either horizontally or vertically distributed on the surface of

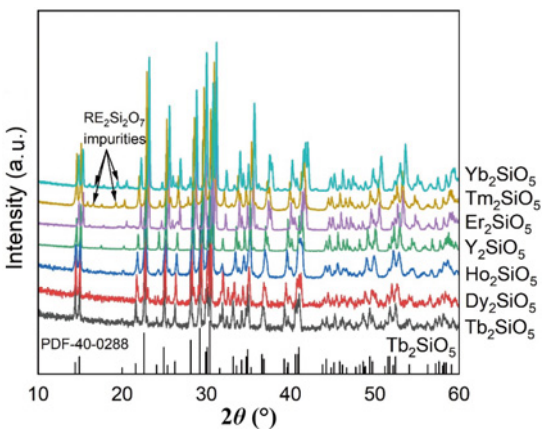

Fig. 1 XRD patterns of as-prepared RE_2SiO_5 (RE = Tb, Dy, Ho, Y, Er, Tm, and Yb).

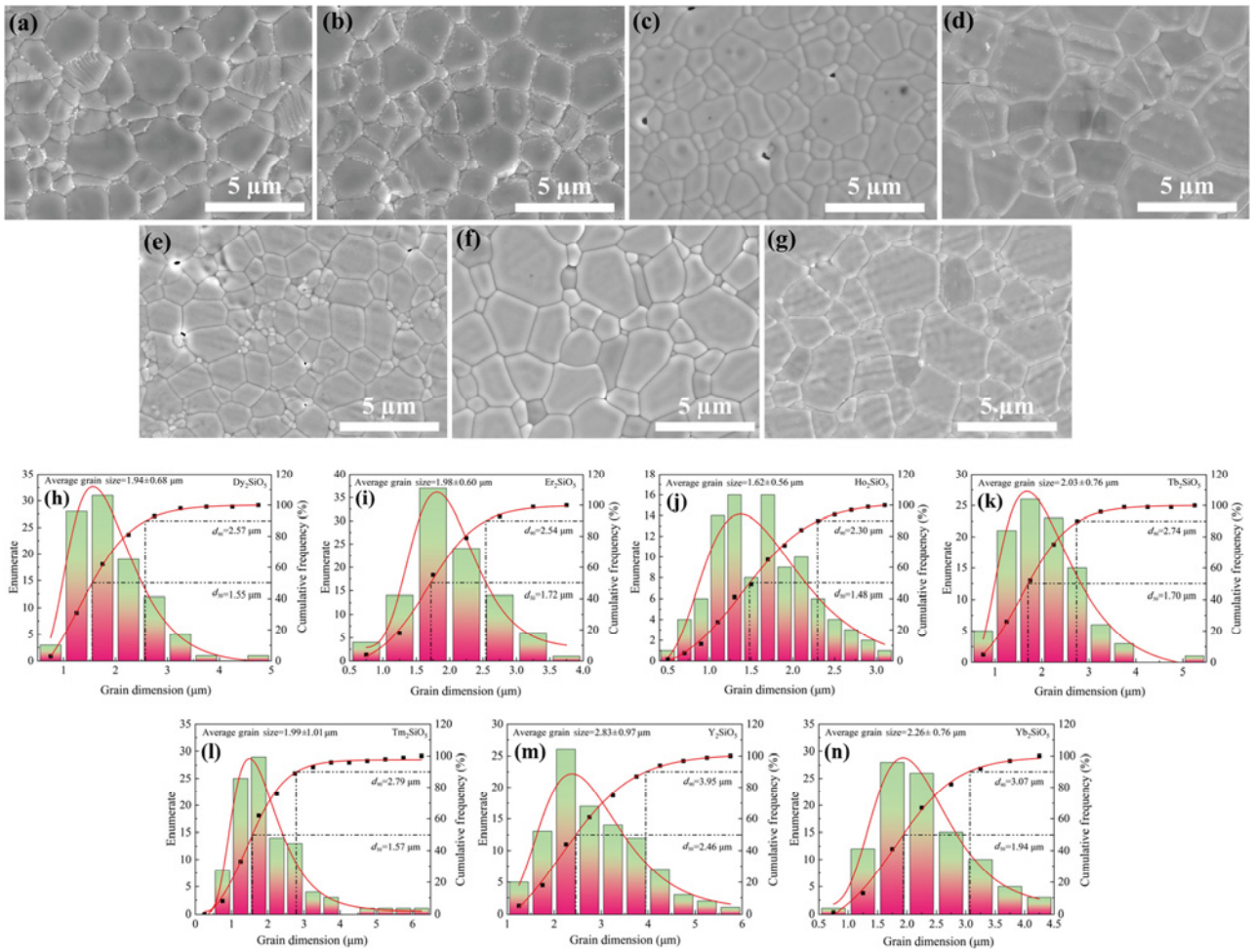

Fig. 2 (a–g) Microstructures of RE_2SiO_5 (RE = Tb, Dy, Ho, Y, Er, Tm, and Yb) after thermal etching at 1300 ℃, respectively; (h–n) their grain size statistics where d_{50} represents the median particle size distribution and means that 50% of the total particles are smaller than this size, and d_{90} means that 90% of the total particles are smaller than this size.

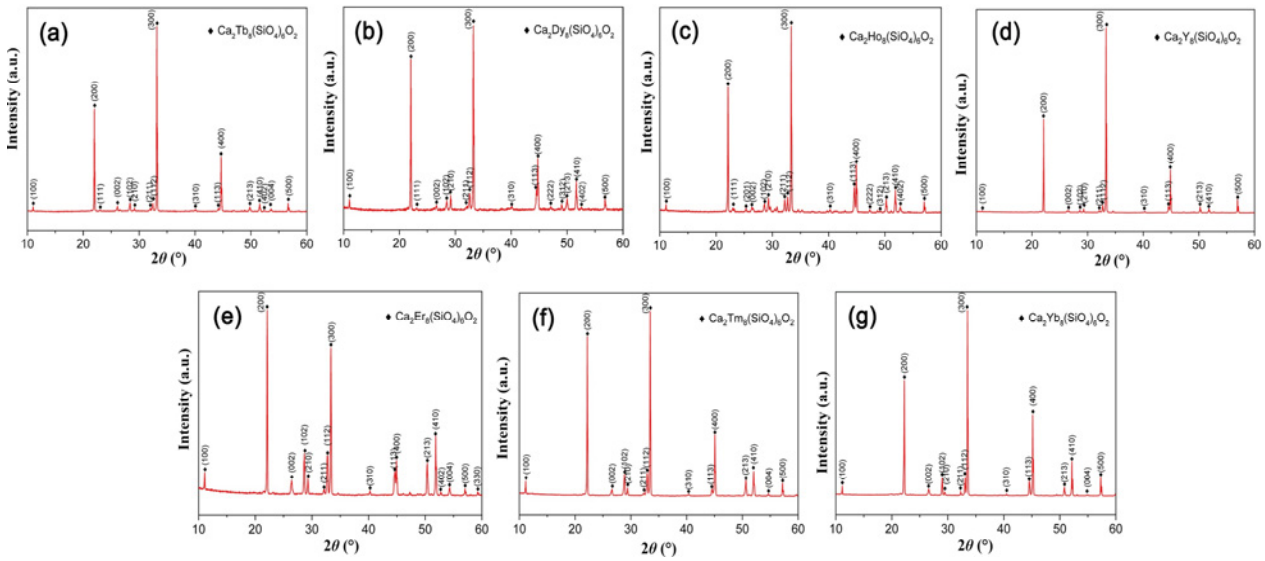

Fig. 3 XRD patterns of (a) Tb_2SiO_5, (b) Dy_2SiO_5, (c) Ho_2SiO_5, (d) Y_2SiO_5, (e) Er_2SiO_5, (f) Tm_2SiO_5, and (g) Yb_2SiO_5 after interaction with CMAS at 1500 ℃ for 5 h.

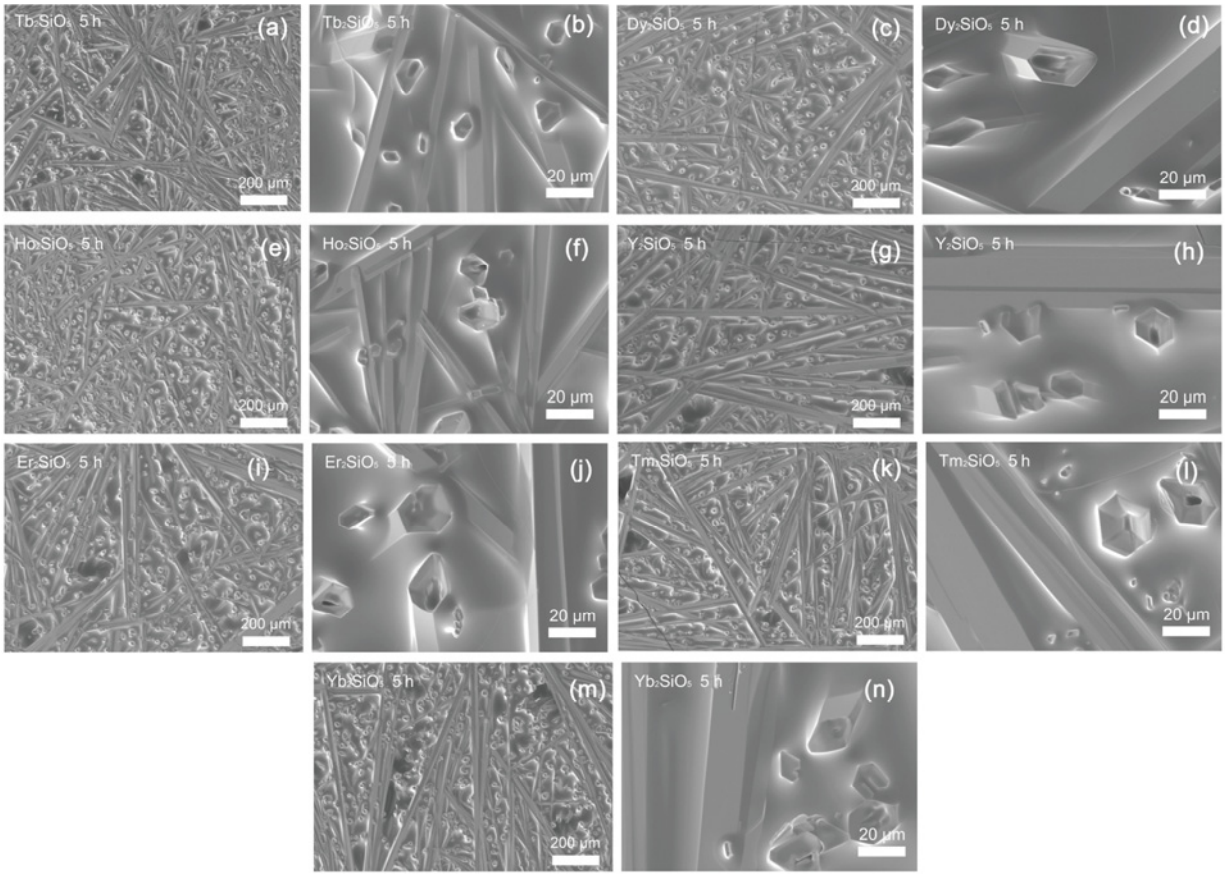

Fig. 4 Surface microstructures of (a, b) Tb_2SiO_5, (c, d) Dy_2SiO_5, (e, f) Ho_2SiO_5, (g, h) Y_2SiO_5, (i, j) Er_2SiO_5, (k, l) Tm_2SiO_5, and (m, n) Yb_2SiO_5 after interaction with CMAS at 1500 ℃ for 5 h.

the RE_2SiO_5 ceramics. The ends of $Ca_2RE_8(SiO_4)_6O_2$ show that they are hexagonal-prismatic grains. In addition, they are filled with a large amount of residual CMAS molten salt, which provides a fast mass transfer channel for the precipitation and growth of the $Ca_2RE_8(SiO_4)_6O_2$. Therefore, the length of $Ca_2RE_8(SiO_4)_6O_2$ is long, even reaching more than 400 μm. Figure 5 presents the corresponding cross-section images of RE_2SiO_5 (RE = Tb, Dy, Ho, Y, Er, Tm, and Yb), and they can be divided into three regions according to the EDS elemental mappings. There is a lot of residual CMAS on the top surface, a thin layer of the reaction zone is in the middle, and the bottom is the RE_2SiO_5 substrate. Most of the reaction products are randomly distributed in the residual CMAS. In Tb_2SiO_5, the reaction zone is almost filled with gradient-distributed hexagonal-prismatic reaction products. The closer to the substrate, the denser the reaction products. Furthermore, the reaction products are confirmed to be $Ca_2Tb_8(SiO_4)_6O_2$ based on the EDS point analysis (Fig. 5(c)). For Dy_2SiO_5, Ho_2SiO_5, Y_2SiO_5, and Er_2SiO_5, the reaction products ($Ca_2RE_8(SiO_4)_6O_2$) are coarse and form a dense layer in the reaction zone. The growth of $Ca_2RE_8(SiO_4)_6O_2$ tends to be impeded by the dense $Ca_2RE_8(SiO_4)_6O_2$ layer which blocks the dissolution of RE_2SiO_5 into CMAS. From the EDS elemental mapping (Fig. 5), a smooth interface between RE_2SiO_5 and $Ca_2RE_8(SiO_4)_6O_2$ (RE = Tb, Dy, Ho, Y, and Er) layer can be observed clearly. However, in Tm_2SiO_5 and Yb_2SiO_5, the interfaces become rough with $Ca_2RE_8(SiO_4)_6O_2$ fringes in the reaction zone.

The interactions between CMAS and RE_2SiO_5 (RE = Dy, Ho, Y, Er, Tm, and Yb) for a longer duration were also investigated. CMAS flowed down the edge of Tb_2SiO_5, and thus it is not presented. Figure 6 illustrates the XRD patterns of RE_2SiO_5 (RE = Dy, Ho, Y, Er, Tm, and Yb) after interaction with CMAS at 1500 ℃ for 20 h. $Ca_2RE_8(SiO_4)_6O_2$ are detected in all RE_2SiO_5 and their XRD patterns are similar. The intensity of (200) and (300) diffraction peaks of $Ca_2RE_8(SiO_4)_6O_2$ (RE = Dy, Ho, Y, Er, Tm, and Yb) is much stronger than other diffraction peaks, which are quite similar to that of $Ca_2RE_8(SiO_4)_6O_2$ (RE = Dy, Ho, Y, Er, Tm, and Yb) forming at 1500 ℃ for 5 h.

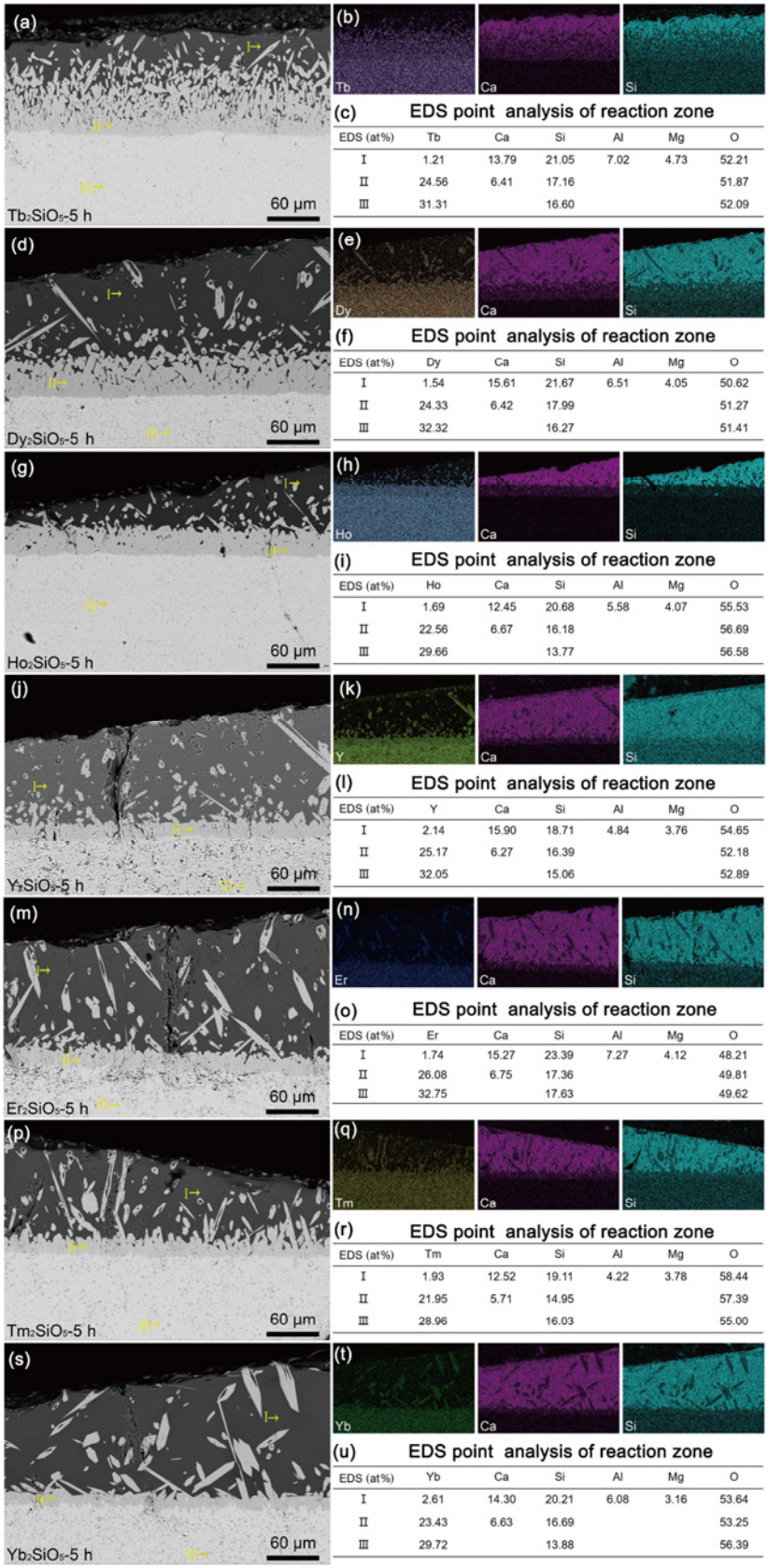

Fig. 5 Cross-sectional images and EDS elemental mapping of (a–c) Tb_2SiO_5, (d–f) Dy_2SiO_5, (g–i) Ho_2SiO_5, (j–l) Y_2SiO_5, (m–o) Er_2SiO_5, (p–r) Tm_2SiO_5, and (s–u) Yb_2SiO_5 after interaction with CMAS at 1500 ℃ for 5 h.

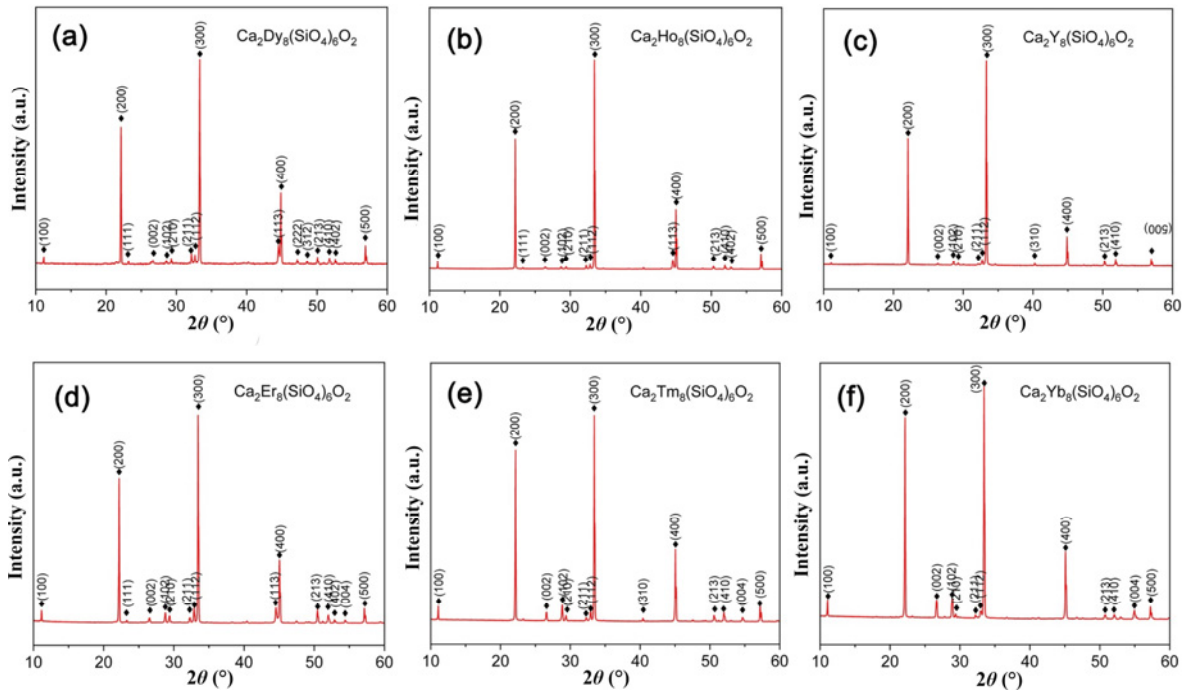

Fig. 6 XRD patterns of (a) Dy_2SiO_5, (b) Ho_2SiO_5, (c) Y_2SiO_5, (d) Er_2SiO_5, (e) Tm_2SiO_5, and (f) Yb_2SiO_5 after interaction with CMAS at 1500 ℃ for 20 h.

Figure 7 displays the surface microstructures of RE_2SiO_5 (RE = Dy, Ho, Y, Er, Tm, and Yb) after CMAS corrosion at 1500 ℃ for 20 h. $Ca_2RE_8(SiO_4)_6O_2$ are hexagonal-prismatic grains vertically or horizontally distributed in the residual CMAS. To reveal the resistance to CMAS corrosion, cross-section images of RE_2SiO_5 (RE = Dy, Ho, Y, Er, Tm, and Yb) are illustrated in Fig. 8. $Ca_2RE_8(SiO_4)_6O_2$ grains accumulate at the bottom of CMAS constructing a dense layer. The interfaces between RE_2SiO_5 substrate and $Ca_2RE_8(SiO_4)_6O_2$ layer are flat in Dy_2SiO_5, Ho_2SiO_5, Y_2SiO_5, and Er_2SiO_5. However, in Tm_2SiO_5 and Yb_2SiO_5, $Ca_2RE_8(SiO_4)_6O_2$ grains tend to grow into the RE_2SiO_5 substrate and some protruding grains are visible.

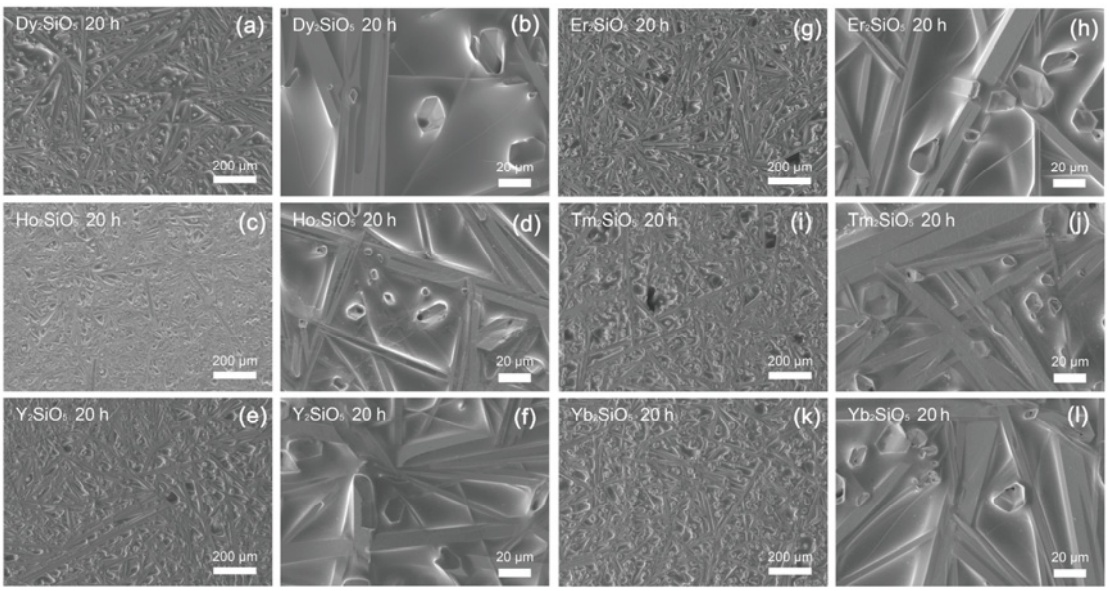

Fig. 7 Surface microstructures of (a, b) Dy_2SiO_5, (c, d) Ho_2SiO_5, (e, f) Y_2SiO_5, (g, h) Er_2SiO_5, (i, j) Tm_2SiO_5, and (k, l) Yb_2SiO_5, after interaction with CMAS at 1500 ℃ for 20 h.

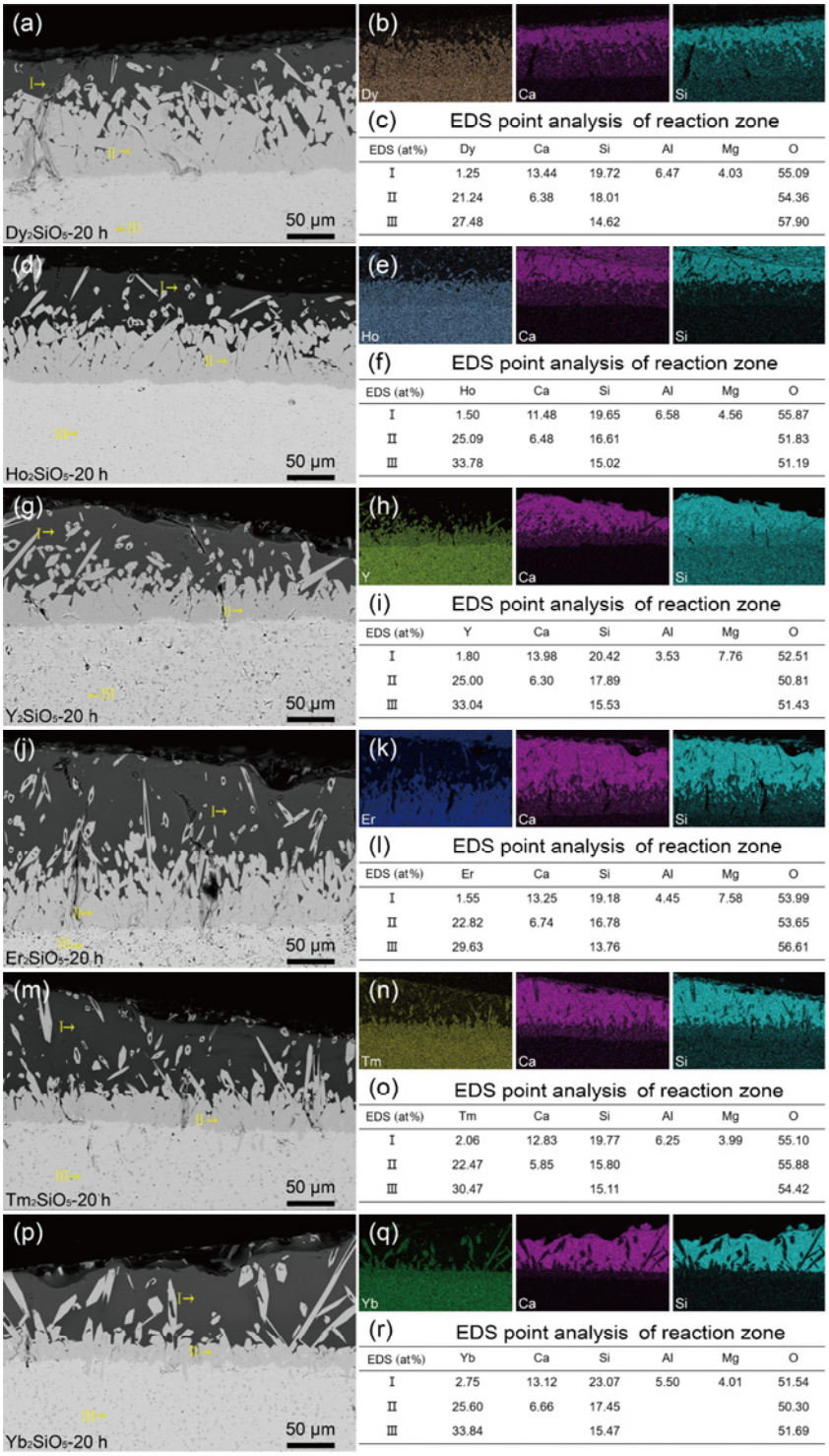

Fig. 8 Cross-section images and EDS elemental mapping of (a–c) Dy_2SiO_5, (d–f) Ho_2SiO_5, (g–i) Y_2SiO_5, (j–l) Er_2SiO_5, (m–o) Tm_2SiO_5, and (p–r) Yb_2SiO_5 after interaction with CMAS at 1500 ℃ for 20 h.

XRD patterns of RE_2SiO_5 (RE = Y, Er, Tm, and Yb) after interaction with CMAS for 50 h at 1500 ℃ are presented in Fig. 9. CMAS flowed down the surface of Tb_2SiO_5, Dy_2SiO_5, and Ho_2SiO_5, so their CMAS corrosion behaviors are not presented. Figure 10 and Movie S1 in the Electronic Supplementary Material (ESM) show the evolution of CMAS molten salt on Ho_2SiO_5 at high temperatures. Bulk CMAS was placed on the top of Ho_2SiO_5. As the temperature increases, CMAS will melt and spread on the sample surface.

A camera was used to record the changes in the shape of CMAS and to analyze the corrosion process. CMAS starts to melt at 1310 ℃ and becomes a dome-like droplet at 1330 ℃. With the increase in temperature, CMAS wets the entire surface of Ho_2SiO_5 at 1350 ℃. However, at 1405 ℃, it begins to flow down the edge of the Ho_2SiO_5 and the corrosion will terminate due to the shortage of CMAS melts. At 1475 ℃, the phenomenon of CMAS molten salt undulation can be seen, indicating a more vigorous corrosion reaction. Therefore, the better wettability of CMAS on surfaces of RE_2SiO_5 with larger RE cations causes it to flow down the edge of the sample easily. The interactions between CMAS and Tb_2SiO_5, Dy_2SiO_5, and Ho_2SiO_5 at 1500 ℃ for 50 h were not shown due to the loss of CMAS. Figure 9 determines that $Ca_2RE_8(SiO_4)_6O_2$ are the main reaction products, and the XRD patterns are consistent well with those in Fig. 6. Intensity of the (200) and (300) diffraction peaks of $Ca_2RE_8(SiO_4)_6O_2$ (RE = Y, Er, Tm, and Yb) are still relatively strong. Figure 11 shows the surface microstructures of RE_2SiO_5 (RE = Y, Er, Tm, and Yb) after CMAS corrosion at 1500 ℃ for 50 h. A lot of hexagonal-prismatic $Ca_2RE_8(SiO_4)_6O_2$ grains are randomly dispersed in the residual CMAS on the top of Y_2SiO_5, Er_2SiO_5, Tm_2SiO_5, and Yb_2SiO_5. Figure 12 illustrates the corresponding cross-sectional images of RE_2SiO_5 (RE = Y, Er, Tm, and Yb), and the residual CMAS remains on the surface of Y_2SiO_5, Er_2SiO_5, Tm_2SiO_5, and Yb_2SiO_5, but they become less than those performed for 5 and 20 h. The $Ca_2RE_8(SiO_4)_6O_2$ layers are thick and dense due to long-term interactions with CMAS. The interfaces between the reaction zone and RE_2SiO_5 substrate are flat for Y_2SiO_5 and Er_2SiO_5, but rough for Tm_2SiO_5 and Yb_2SiO_5. Some $Ca_2RE_8(SiO_4)_6O_2$ in Tm_2SiO_5 and Yb_2SiO_5 even penetrates into the RE_2SiO_5 substrate.

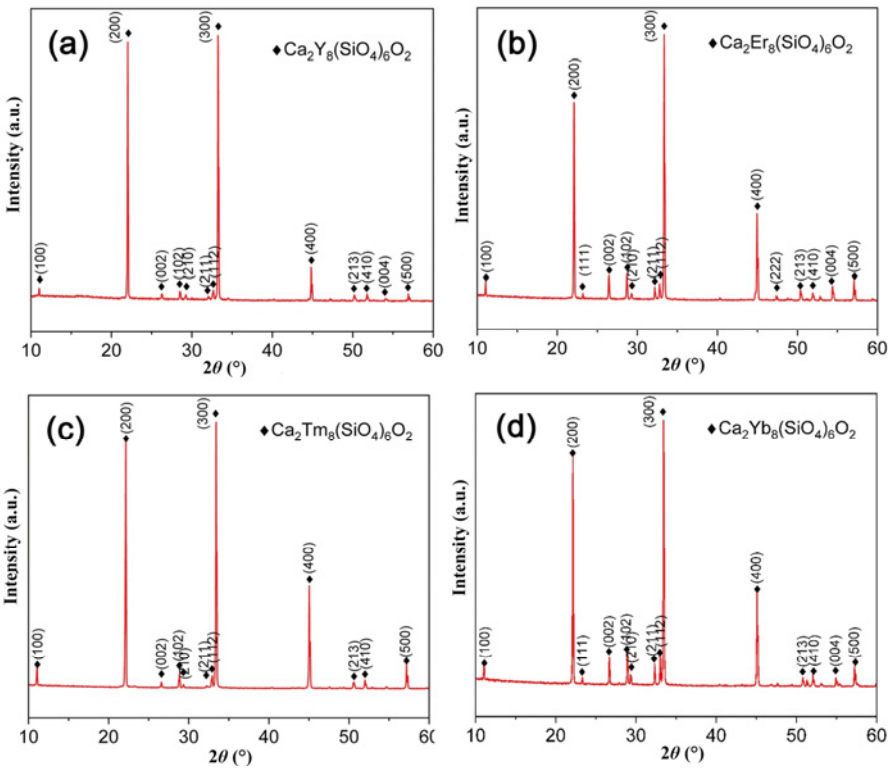

Fig. 9 XRD patterns of (a) Y_2SiO_5, (b) Er_2SiO_5, (c) Tm_2SiO_5, and (d) Yb_2SiO_5 after interaction with CMAS at 1500 ℃ for 50 h.

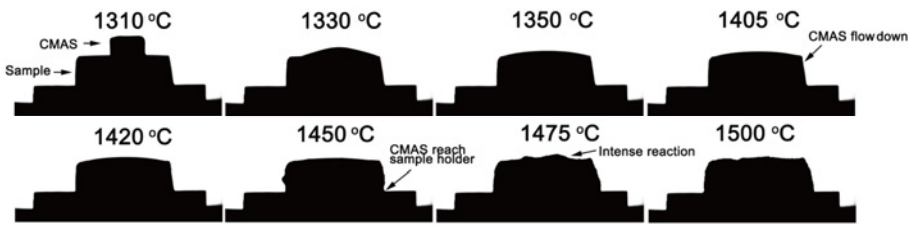

Fig. 10 Evolution of CMAS on Ho_2SiO_5 at high temperatures.

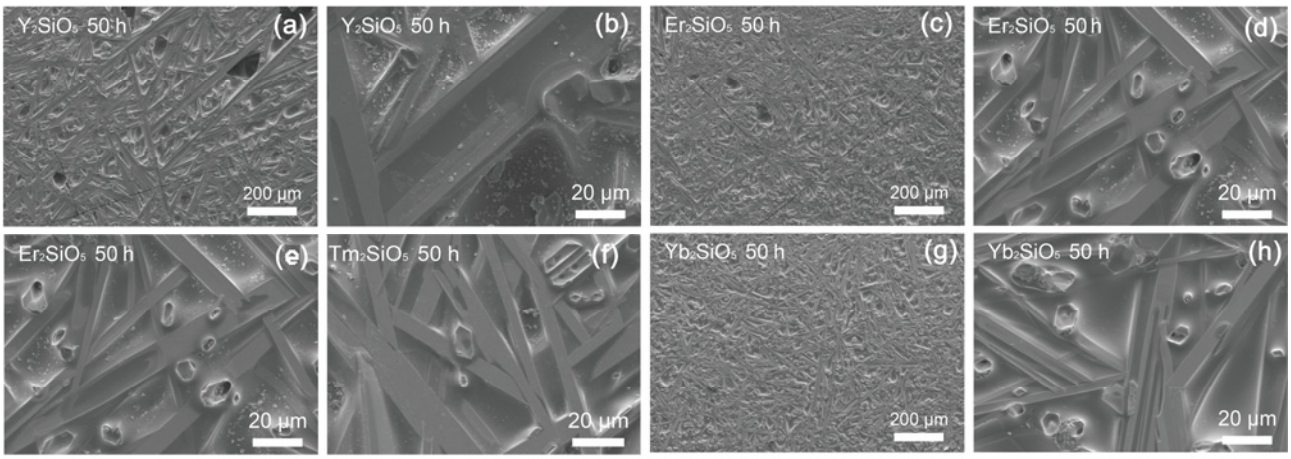

Fig. 11 Surface microstructures of (a, b) Y_2SiO_5, (c, d) Er_2SiO_5, (e, f) Tm_2SiO_5, and (g, h) Yb_2SiO_5 after interaction with CMAS at 1500 ℃ for 50 h.

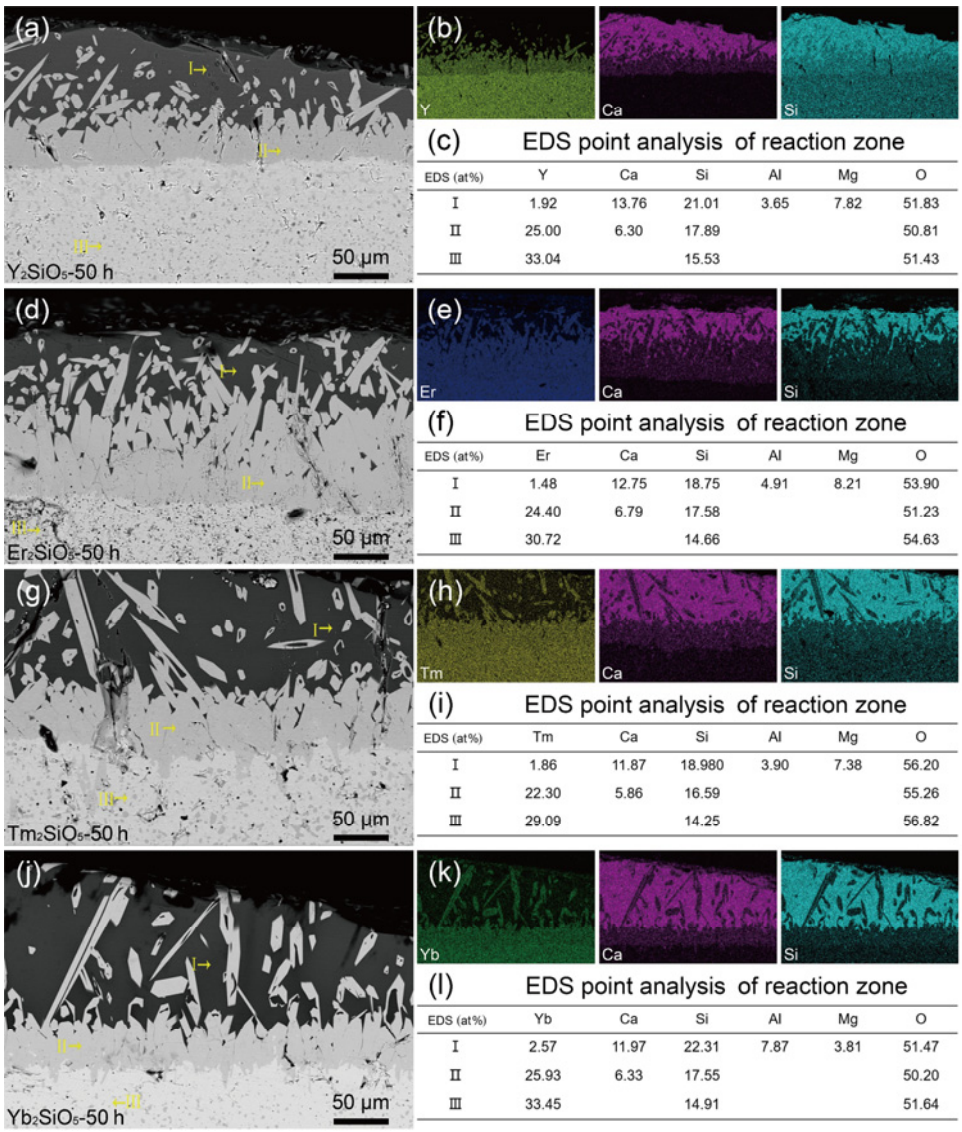

Fig. 12 Cross-sectional images and EDS elemental mapping of (a–c) Y_2SiO_5, (d–f) Er_2SiO_5, (g–i) Tm_2SiO_5, and (j–l) Yb_2SiO_5 after interaction with CMAS at 1500 ℃ for 50 h.

4 Discussion

4. 1 Preferential growth of $Ca_2RE_8(SiO_4)_6O_2$

$Ca_2RE_8(SiO_4)_6O_2$ are the main reaction products of RE_2SiO_5 (RE = Tb, Dy, Ho, Y, Er, Tm, and Yb) after interaction with CMAS at 1500 ℃. $Ca_2RE_8(SiO_4)_6O_2$ crystallizes into the hexagonal space group *P*63/*m* and it contains [SiO_4] tetrahedral, [(RE/Ca)O_x] polyhedral, and [REO_x] polyhedral units (Fig. 13(a)) [30]. Figure 14 shows surface morphologies of RE_2SiO_5 (RE = Tb, Dy, Ho, Y, Er, Tm, and Yb) after corrosion by CMAS at 1500 ℃. It can be seen that $Ca_2RE_8(SiO_4)_6O_2$ (RE = Tb, Dy, Ho, Y, Er, Tm, and Yb) are randomly distributed. According to the XRD patterns with strong intensity of (200) and (300) diffraction peaks, $Ca_2RE_8(SiO_4)_6O_2$ (RE = Tb, Dy, Ho, Y, Er, Tm, and Yb) should grow faster in the [001] direction leading to long hexagonal-prismatic grains with preferential (100) facets exposed (Fig. 13(b)). Therefore, the increased intensities of some specific diffraction peaks in the XRD patterns of $Ca_2RE_8(SiO_4)_6O_2$ originate from different preferential growth mechanisms.

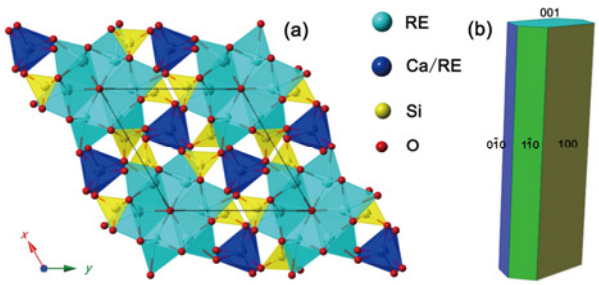

Fig. 13 (a) Crystal structure and (b) schematic diagram of preferential grain growth of $Ca_2RE_8(SiO_4)_6O_2$.

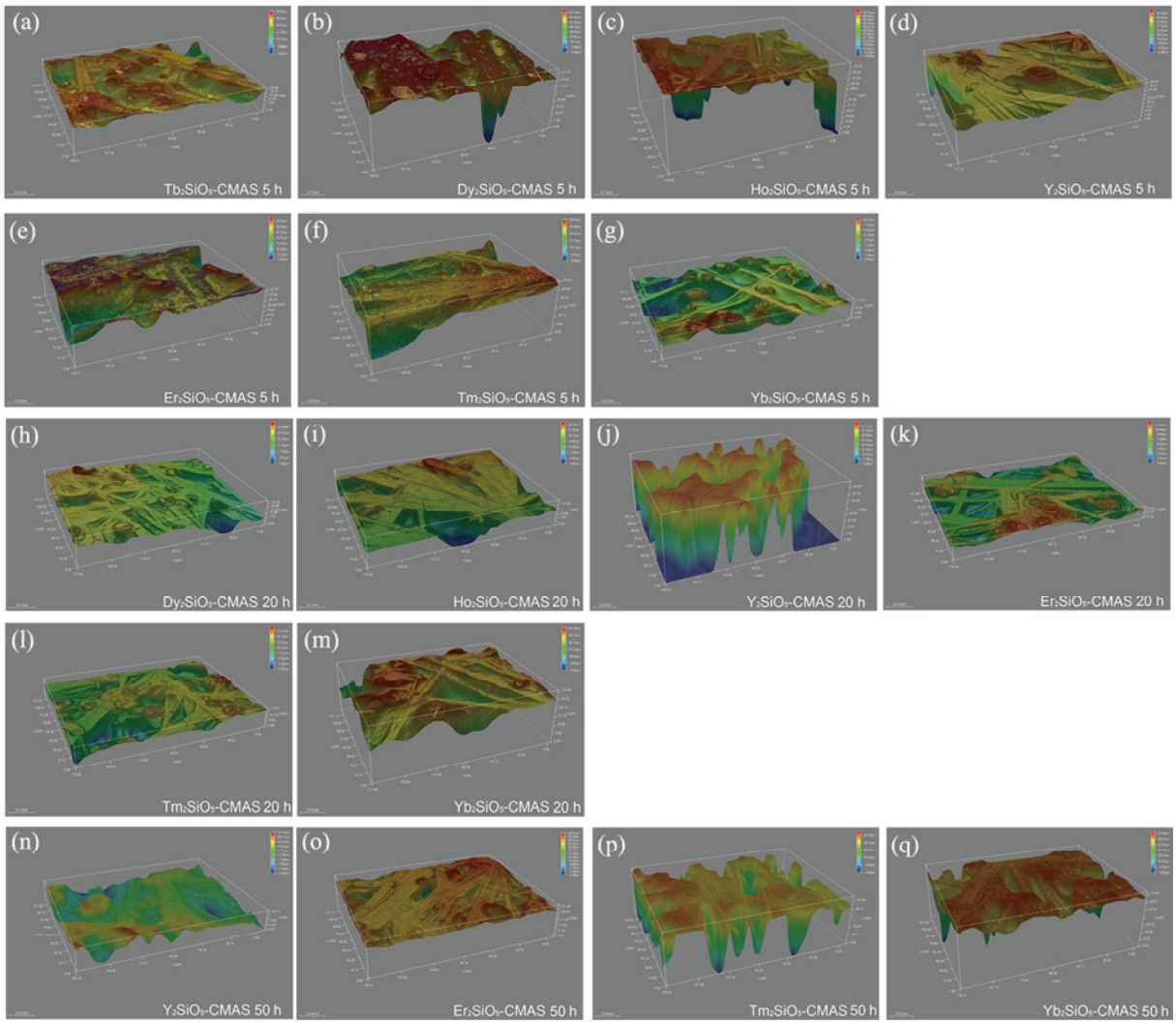

Fig. 14 Surface microstructure of RE_2SiO_5 (RE = Tb, Dy, Ho, Y, Er, Tm, and Yb) after interaction with CMAS at 1500 ℃ for (a–g) 5 h, (h–m) 20 h, and (n–q) 50 h.

To reveal the precipitation mechanism of $Ca_2RE_8(SiO_4)_6O_2$, *in-situ* observation of high-temperature interactions of Er_2SiO_5 with CMAS was performed. The interaction process was recorded and shown in Movie S2 in the ESM. CMAS melted at about 1300 ℃ and presented good flowability. $Ca_2Er_8(SiO_4)_6O_2$ slowly precipitated after interaction of about 1 h with CMAS at 1500 ℃. $Ca_2Er_8(SiO_4)_6O_2$ grains can flow in the molten salt. With the increase in the duration of corrosion, $Ca_2Er_8(SiO_4)_6O_2$ grains continued to grow and became thicker and longer (Figs. 15(a) and 15(b)), suggesting the interaction was mild. During the cooling process, a large amount of $Ca_2Er_8(SiO_4)_6O_2$ grains with a length of about 50–100 μm started to precipitate horizontally from the residual CMAS melts when the temperature decreased to 1400 ℃ (Fig. 15(c)). It indicated that the saturation of $ErO_{1.5}$ in CMAS molten salt decreased with decreasing temperature, and the cooling process promoted the precipitation of $Ca_2Er_8(SiO_4)_6O_2$. Therefore, long $Ca_2Er_8(SiO_4)_6O_2$ grains should form at a high- temperature corrosion stage (> 1400 ℃), and most short and horizontal $Ca_2Er_8(SiO_4)_6O_2$ grains precipitated during the cooling process.

In addition, the interaction process between Er_2SiO_5 and CMAS at 1300 ℃ was also monitored, shown in Figs. 15(d) and 15(f) and Movie S3 in the ESM. No $Ca_2Er_8(SiO_4)_6O_2$ was observed in the molten melts after interaction for about 2.5 h which was different from the corrosion test conducted at 1500 ℃. Previous investigation shows that Er_2SiO_5 presents mild corrosion when attacked by CMAS at 1300 ℃ for 50 h [25]. A lot of residual CMAS was left on the top of Er_2SiO_5 indicating an inert reaction with CMAS consistent with the *in-situ* observation results. In addition, the viscosity of CMAS as a function of the temperature was calculated by the Factsage software and shown in Fig. 16. The viscosity of CMAS at 1300 ℃ is more than four times higher than that of 1500 ℃. The low viscosity at 1500 ℃ promotes mass transfer and allows $Ca_2RE_8(SiO_4)_6O_2$ grains to grow freely. $Ca_2RE_8(SiO_4)_6O_2$ grains can grow rapidly along the radial direction while constantly adjusting their orientation without constraint.

Moreover, according to Arrhenius equation, the chemical reaction rate constant (ζ) is written as Eq. (1):

$$\zeta = A\exp(-E/(RT)) \quad (1)$$

where A is the pre-exponential factor, T is the temperature, E denotes the activation energy of corrosion dissolution, and R is the gas constant. High

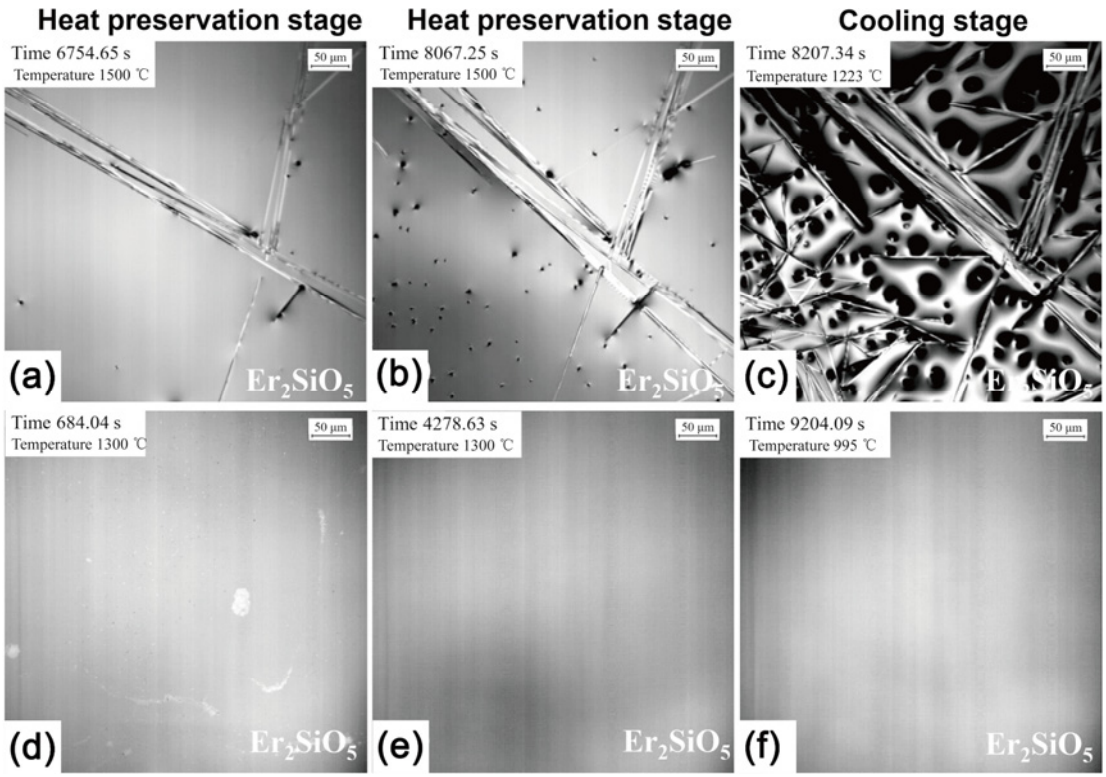

Fig. 15 *In situ* observation of CMAS interaction with (a–c) Er_2SiO_5 at 1500 ℃ and (d–f) Er_2SiO_5 at 1300 ℃.

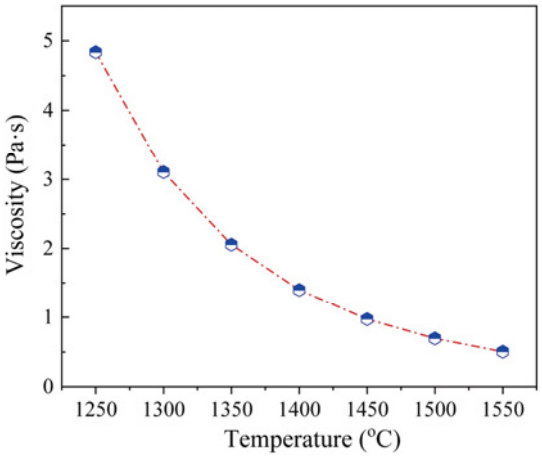

Fig. 16 Viscosity of CMAS as a function of temperature.

temperatures can increase the chemical reaction rate leading to an active corrosion reaction. Therefore, the reaction between CMAS and RE_2SiO_5 at high temperatures should be controlled by the solubility of $REO_{1.5}$ and the chemical reaction rate constant.

Furthermore, the size of $Ca_2RE_8(SiO_4)_6O_2$ grains forming at 1500 ℃ is much larger than that created at 1300 ℃. For instance, the $Ca_2Tb_8(SiO_4)_6O_2$ grains forming on the top surface of Tb_2SiO_5 are much longer than that occurring at 1300 ℃ for 50 h (Fig. 17). Thus, high temperatures effectively promote the preferential growth of $Ca_2RE_8(SiO_4)_6O_2$.

4. 2 Influence of RE elements on CMAS resistance of RE_2SiO_5

The CMAS infiltration depths of RE_2SiO_5 (RE = Tb, Dy, Ho, Y, Er, Tm, and Yb) at 1500 ℃ are measured from the original surface to the deepest position of CMAS infiltration (Figs. S1–S3 in the ESM). Figure 18(a) illustrates the relationship between the CMAS infiltration depths and the radius of RE^{3+}. The CMAS infiltration depths increase slowly with the decrease of the radius of RE^{3+}. The CMAS infiltration depths are close for the RE_2SiO_5 ceramics when performed at 1500 ℃. When the RE_2SiO_5 (RE = Tb, Dy, Ho, Y, Er, Tm, and Yb) ceramics were attacked by CMAS at 1300 ℃, the infiltration depths almost linearly decreased with the reduction of the radius of RE^{3+} [25]. Costa *et al.* [31] found that the enthalpy of formation from $Ca_2RE_8(SiO_4)_6O_2$ becomes more exothermic as the ionic radius of the RE elements increases. The smaller the RE ionic radius the less likely to generate $Ca_2RE_8(SiO_4)_6O_2$ corrosion products. Therefore, RE_2SiO_5 (RE = Tb, Dy, Ho, Y, Er, Tm, and Yb) presents linear resistance to CMAS at 1300 ℃ depending on the formation enthalpy of corrosion products. When the operating temperature rises to 1500 ℃, the viscosity of the CMAS molten salt is greatly reduced which accelerates the mass transfer. In addition, the corrosion reaction becomes violent which can be seen in Fig. 10. According to Arrhenius equation, the corrosion reaction rate will also accelerate as the temperature increases. The difference in the ability of RE_2SiO_5 to form corrosion products is decreasing, leading to a small difference in their CMAS corrosion resistance. Figure 18(b) shows the time-dependent CMAS infiltration depths for different RE_2SiO_5. The CMAS penetration depths increase slowly for RE_2SiO_5 with larger RE cations. The dense $Ca_2RE_8(SiO_4)_6O_2$ layer in the reaction zone inhibited further corrosion. Compared with the corrosion test performed at 1300 ℃, RE_2SiO_5 (RE = Tb, Dy, Ho, Y, Er, Tm, and Yb) exhibits fast interaction with CMAS at 1500 ℃, and the influence of RE species on the CMAS resistance is not as significant as that conducted at 1300 ℃.

4. 3 Influence of grain size and porosity on CMAS resistance of RE_2SiO_5

CMAS infiltrates along grain boundaries have been found in yttria-stabilized zirconia [32], where the smaller the grain size the more grain boundaries there

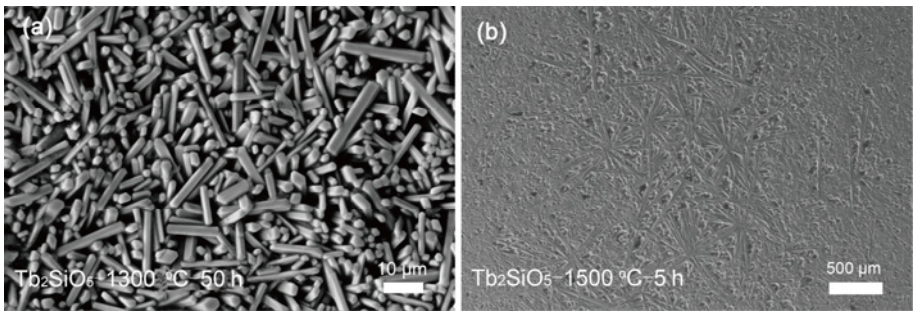

Fig. 17 Comparison of microstructures of $Ca_2Tb_8(SiO_4)_6O_2$ forming at (a) 1300 ℃ for 50 h and (b) 1500 ℃ for 5 h.

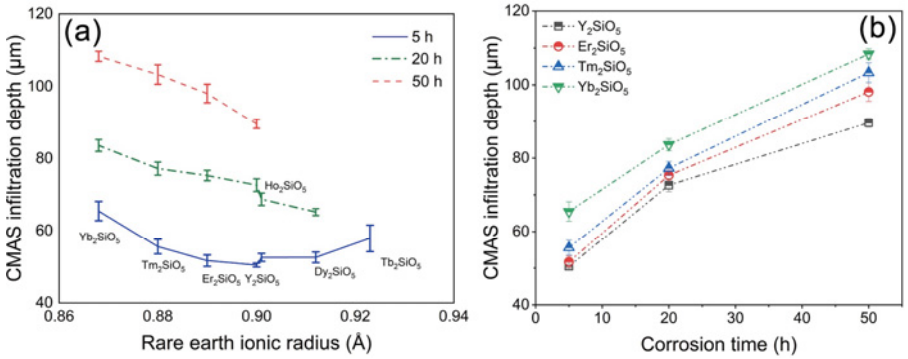

Fig. 18 Infiltration depths of CMAS as a function of (a) radius of RE^{3+} and (b) duration of corrosion.

are. The paths for CMAS to penetrate along the grain boundaries are more abundant, and the materials are more likely to exhibit poorer corrosion resistance. However, no significant grain boundary corrosion was found in the RE_2SiO_5 ceramics and the difference in grain size is small. Thus, the effect of the grain size on CMAS corrosion is weak. In addition, pressureless sintering makes it difficult to avoid the presence of pores in the sample. Connecting pores can provide a reservoir for CMAS melts when interacting with RE_2SiO_5, which will facilitate the penetration of CMAS. However, in this work, the porosity of Tb_2SiO_5, Dy_2SiO_5, Ho_2SiO_5, Y_2SiO_5, Er_2SiO_5, Tm_2SiO_5, and Yb_2SiO_5 are 7.7%, 3.6%, 4.1%, 4.8%, 6.9%, 3.1%, and 4.5%, respectively. The RE_2SiO_5 samples are dense without a large number of pores as shown in Fig. 2. The existing pores are isolated close pores which will not promote the CMAS infiltration. Therefore, no CMAS accumulation was found in the cross-section of the sample. In addition, few cracks were detected in the sample. It is believed that few pores and cracks have a weak effect on the CMAS penetration.

5 Conclusions

The interactions between CMAS and RE_2SiO_5 (RE = Tb, Dy, Ho, Y, Er, Tm, and Yb) at 1500 ℃ for 5, 20, and 50 h were comprehensively investigated. Influences of the high temperature and compositions of RE_2SiO_5 on their CMAS resistance were revealed. The high temperature promotes the growth of the reaction products $Ca_2RE_8(SiO_4)_6O_2$. They grow fast along [001] with preferentially exposed (100) facets and are randomly distributed. The cooling process accelerates the precipitation of short and horizontally distributed $Ca_2RE_8(SiO_4)_6O_2$ grains. CMAS infiltration depths of RE_2SiO_5 (RE = Tb, Dy, Ho, Y, Er, Tm, and Yb) ceramics slowly increase with the reduction of the radius of RE^{3+}. The RE_2SiO_5 (RE = Tb, Dy, Ho, Y, Er, Tm, and Yb) ceramics with large RE cations show better CMAS resistance at 1500 ℃. This study clarifies the effect of critical factors on the resistance to CMAS of RE_2SiO_5 at 1500 ℃, and the results provide guidelines for CMAS-resistant rare earth silicate EBCs.

Acknowledgements

This work was financially supported by the National Natural Science Foundation of China (Grant Nos. 52202078 and 52202126), Guangdong Basic and Applied Basic Research Foundation for Distinguished Young Scholars (Grant No. 2021B1515020083), Guangdong Basic and Applied Basic Research Foundation (Grant Nos. 2021A1515110293 and 2022A1515012201), and Shenzhen Science and Technology Program (Grant Nos. 202206193000001 and 20220818183014003).

Declaration of competing interest

The authors have no competing interests to declare that are relevant to the content of this article The author Jingyang Wang is the Editorial Committee member of this journal.

Electronic Supplementary Material

Supplementary material is available in the online version of this article at https://doi.org/10.26599/JAC.2023.9220822.

References

[1] Padture NP. Advanced structural ceramics in aerospace

propulsion. *Nat Mater* 2016, **15**: 804–809.
[2] Lv XR, Yue MK, Feng X, *et al*. Rare earth monosilicates as oxidation resistant interphase for SiC_f /SiC CMC: Investigation of SiC_f/Yb_2SiO_5 model composites. *J Adv Ceram* 2022, **11**: 702–711.
[3] Yang LW, Xiao XR, Liu LP, *et al*. Dynamic oxidation mechanism of carbon fiber reinforced SiC matrix composite in high-enthalpy and high-speed plasmas. *J Adv Ceram* 2022, **11**: 365–377.
[4] Padture NP. Environmental degradation of high-temperature protective coatings for ceramic-matrix composites in gas-turbine engines. *npj Mater Degrad* 2019, **3**: 11.
[5] Tejero-Martin D, Bennett C, Hussain T. A review on environmental barrier coatings: History, current state of the art and future developments. *J Eur Ceram Soc* 2021, **41**: 1747–1768.
[6] Lee KN, Fox DS, Bansal NP. Rare earth silicate environmental barrier coatings for SiC/SiC composites and Si_3N_4 ceramics. *J Eur Ceram Soc* 2005, **25**: 1705–1715.
[7] Tian ZL, Zheng LY, Wang JM, *et al*. Theoretical and experimental determination of the major thermo-mechanical properties of RE_2SiO_5 (RE = Tb, Dy, Ho, Er, Tm, Yb, Lu, and Y) for environmental and thermal barrier coating applications. *J Eur Ceram Soc* 2016, **36**: 189–202.
[8] Tian ZL, Lin CF, Zheng LY, *et al*. Defect-mediated multiple-enhancement of phonon scattering and decrement of thermal conductivity in $(Y_xYb_{1-x})_2SiO_5$ solid solution. *Acta Mater* 2018, **144**: 292–304.
[9] Xu Y, Hu XX, Xu FF, *et al*. Rare earth silicate environmental barrier coatings: Present status and prospective. *Ceram Int* 2017, **43**: 5847–5855.
[10] Drexler JM, Gledhill AD, Shinoda K, *et al*. Jet engine coatings for resisting volcanic ash damage. *Adv Mater* 2011, **23**: 2419–2424.
[11] Guo L, Li G, Wu J, *et al*. Effects of pellet surface roughness and pre-oxidation temperature on CMAS corrosion behavior of Ti_2AlC. *J Adv Ceram* 2022, **11**: 945–960.
[12] Levi CG, Hutchinson JW, Vidal-Sétif MH, *et al*. Environmental degradation of thermal-barrier coatings by molten deposits. *MRS Bull* 2012, **37**: 932–941.
[13] Wolf M, Mack DE, Guillon O, *et al*. Resistance of pure and mixed rare earth silicates against calcium–magnesium–aluminosilicate (CMAS): A comparative study. *J Am Ceram Soc* 2020, **103**: 7056–7071.
[14] Poerschke DL, Shaw JH, Verma N, *et al*. Interaction of yttrium disilicate environmental barrier coatings with calcium–magnesium-iron alumino–silicate melts. *Acta Mater* 2018, **145**: 451–461.
[15] Zhao HB, Richards BT, Levi CG, *et al*. Molten silicate reactions with plasma sprayed ytterbium silicate coatings. *Surf Coat Technol* 2016, **288**: 151–162.
[16] Grant KM, Krämer S, Seward GGE, *et al*. Calcium–magnesium alumino–silicate interaction with yttrium monosilicate environmental barrier coatings. *J Am Ceram Soc* 2010, **93**: 3504–3511.
[17] Poerschke DL, Hass DD, Eustis S, *et al*. Stability and CMAS resistance of ytterbium–silicate/hafnate EBCs/TBC for SiC composites. *J Am Ceram Soc* 2015, **98**: 278–286.
[18] Tian ZL, Zhang J, Zhang TY, *et al*. Towards thermal barrier coating application for rare earth silicates RE_2SiO_5 (RE = La, Nd, Sm, Eu, and Gd). *J Eur Ceram Soc* 2019, **39**: 1463–1476.
[19] Tian ZL, Ren XM, Lei YM, *et al*. Corrosion of $RE_2Si_2O_7$ (RE = Y, Yb, and Lu) environmental barrier coating materials by molten calcium–magnesium–alumino–silicate glass at high temperatures. *J Eur Ceram Soc* 2019, **39**: 4245–4254.
[20] Wiesner VL, Scales D, Johnson NS, *et al*. Calcium–magnesium aluminosilicate (CMAS) interactions with ytterbium silicate environmental barrier coating material at elevated temperatures. *Ceram Int* 2020, **46**: 16733–16742.
[21] Turcer LR, Krause AR, Garces HF, *et al*. Environmental-barrier coating ceramics for resistance against attack by molten calcia–magnesia–aluminosilicate (CMAS) glass: Part I, $YAlO_3$ and γ-$Y_2Si_2O_7$. *J Eur Ceram Soc* 2018, **38**: 3905–3913.
[22] Chen ZL, Tian ZL, Zheng LY, *et al*. $(Ho_{0.25}Lu_{0.25}Yb_{0.25}Eu_{0.25})_2SiO_5$ high-entropy ceramic with low thermal conductivity, tunable thermal expansion coefficient, and excellent resistance to CMAS corrosion. *J Adv Ceram* 2022, **11**: 1279–1293.
[23] Dong Y, Ren K, Wang QK, *et al*. Interaction of multicomponent disilicate $(Yb_{0.2}Y_{0.2}Lu_{0.2}Sc_{0.2}Gd_{0.2})_2Si_2O_7$ with molten calcia–magnesia–aluminosilicate. *J Adv Ceram* 2022, **11**: 66–74.
[24] Poerschke DL, Jackson RW, Levi CG. Silicate deposit degradation of engineered coatings in gas turbines: Progress toward models and materials solutions. *Annu Rev Mater Res* 2017, **47**: 297–330.
[25] Tian ZL, Zhang J, Zheng LY, *et al*. General trend on the phase stability and corrosion resistance of rare earth monosilicates to molten calcium–magnesium–aluminosilicate at 1300 ℃. *Corros Sci* 2019, **148**: 281–292.
[26] Turcer LR, Krause AR, Garces HF, *et al*. Environmental-barrier coating ceramics for resistance against attack by molten calcia-magnesia-aluminosilicate (CMAS) glass: Part II, β-$Yb_2Si_2O_7$ and β-$Sc_2Si_2O_7$. *J Eur Ceram Soc* 2018, **38**: 3914–3924.
[27] Zhu DM. Development and performance evaluations of HfO_2–Si and rare earth–Si based environmental barrier bond coat systems for SiC/SiC ceramic matrix composites. In: Proceedings of the 41st International Conference on Metallurgical Coatings and Thin Films, 2014.
[28] Cao G, Wang SQ, Wang YH, *et al*. Growth kinetics of apatite layer evolved from calcia–magnesia–aluminosilicate (CMAS) hot corrosion reaction of $(Y_{1-x}Yb_x)_2SiO_5$ ceramics at elevated temperatures of 1673 K and 1773 K. *J Eur Ceram Soc* 2023, **43**: 600–611.
[29] Wu NN, Wang YL, Tong YL, *et al*. Interaction of ytterbium monosilicate environmental barrier coating

material with molten calcium–magnesium–aluminosilicate (CMAS). *Corros Sci* 2023, **211**: 110864.

[30] Chong S, Riley BJ, Nienhuis ET, *et al*. Syntheses and crystal structures of rare-earth oxyapatites $Ca_2RE_8(SiO_4)_6O_2$ (RE = Pr, Tb, Ho, Tm). *J Chem Crystallogr* 2021, **51**: 293–300.

[31] Costa G, Harder BJ, Bansal NP, *et al*. Thermochemistry of calcium rare-earth silicate oxyapatites. *J Am Ceram Soc* 2020, **103**: 1446–1453.

[32] Wu D, Shan X, Cai HY, *et al*. Grain boundary corrosion mechanism of YSZ thermal barrier oxides under CMAS attack. *Corros Sci* 2022, **209**: 110803.